# Modeling the effects of gravity wave momentum deposition on the general circulation above the turbopause

Erdal Yiğit,[1,2] Alexander S. Medvedev,[2] Alan D. Aylward,[1] Paul Hartogh,[2] and Matthew J. Harris[1]

[1]   A nonlinear spectral gravity wave (GW) drag parameterization systematically accounting for breaking and dissipation in the thermosphere developed by Yiğit et al. (2008) has been implemented into the University College London Coupled Middle Atmosphere-Thermosphere-2 (CMAT2) general circulation model (GCM). The dynamical role of GWs propagating upward from the lower atmosphere has been studied in a series of GCM tests for June solstice conditions. The results suggest that GW drag is not only nonnegligible above the turbopause, but that GWs propagate strongly into the upper thermosphere, and, upon their dissipation, deposit momentum comparable to that of ion drag, at least up to $180–200$ km. The effects of thermospheric GW drag are particularly noticeable in the winter (southern) hemisphere, where weaker westerlies and stronger high-latitude easterlies are simulated well, in agreement with the empirical Horizontal Wind Model (HWM93). The dynamic response in the $F$ region is sensitive to the variations of the source spectrum. However, the spectra commonly employed in middle atmosphere GCMs reproduce the circulation both in the lower and upper thermosphere reasonably well.

## 1.   Introduction

[2]   Vertically propagating small-scale gravity waves (GWs) have significant importance for the energy and momentum budget of the middle atmosphere through their vertical transport of horizontal wave momentum, heating associated with wave dissipation, and diffusive mixing effects. Although there were attempts to explicitly resolve GWs in general circulation models (GCMs) [*Becker and Fritts*, 2006; *Berger*, 2008], incorporation of GW drag parameterizations into GCMs is required for realistic simulations because the majority of small-scale GWs still remains unresolved with typical model discretizations. The dynamical effects of GWs have been extensively studied in the middle atmosphere. Numerous observations have shown that maximum GW activity occurs in the mesosphere and lower thermosphere (MLT). Recently, there have been an increasing number of observational studies demonstrating significant GW activity, possibly of a lower atmospheric origin, above the turbopause [*Djuth et al.*, 2004; *Livneh et al.*, 2007]. The turbopause is the level where eddy diffusion, which dominates the lower atmosphere, equals molecular diffusion, which takes over, and dominates in the upper atmosphere. In the GCM to be described in this paper, it corresponds to $\sim 105$ km (see section 2).

[3]   Comprehensive GCMs are not yet capable of simulating the thermospheric effects of GWs emanating from the lower atmosphere. There are two major possible reasons for this deficiency: (1) The GCMs do not couple the troposphere and the upper atmosphere. (2) They lack an appropriate GW drag parameterization that can realistically account for GW dissipation in the thermosphere. The principal goal of this paper is to assess the role of internal GWs propagating from below on the general circulation of the upper thermosphere. For this, we implement an extended nonlinear spectral GW drag scheme recently developed by *Yiğit et al.* [2008] into the University College London's Coupled Middle Atmosphere-Thermosphere-2 (CMAT2) GCM. With this parameterization we consider only waves originating in the lower atmosphere, and do not account for secondary GW sources within the altitude range of the model. The impact of these waves is studied in a series of numerical experiments by comparing the results with existing empirical distributions. For the first time, momentum deposition specifically by upward propagating GWs of lower atmospheric origin is simulated within the framework of a GCM extending from the tropopause to $F$ region altitudes.

[1]Department of Physics and Astronomy, University College London, London, UK.
[2]Max Planck Institute for Solar System Research, Katlenburg-Lindau, Germany.

[4]   Many observational studies focused on the characterization of GW activity and the effects on the mean flow in the lower and middle atmosphere [*Mitchell et al.*, 1994; *Allen and Vincent*, 1995], and at MLT altitudes [*Mitchell and Howells*, 1998; *Janches et al.*, 2006]. GW characteristics in the middle atmosphere, determined by various observational methods, helped to partially constrain GW drag parameterizations commonly used in GCMs. The instruments used have different temporal and spatial resolutions, leading to differing approaches for describing GW fields. For instance, satellite measurements of temperature fluctuations provide a good global coverage of average GW activity [*Ern et al.*, 2004; *Alexander et al.*, 2008], while ground-based lidar measurements [e.g., *Yang et al.*, 2008] offer high temporal resolution but poor global coverage. Other commonly used techniques are airglow imaging, radars, balloon-borne radiosondes, aircraft, meteor trail, and rocketsonde measurements. The majority of these observations focused on the region up to the upper mesosphere. Recently, incoherent scatter measurements demonstrated signatures of internal GWs in the upper thermosphere [*Oliver et al.*, 1997; *Djuth et al.*, 2004; *Livneh et al.*, 2007]. These observations indicated that the ionosphere at *F* region altitudes is continuously perturbed by internal GWs. The precise origin of these disturbances is sometimes unclear as several mechanisms, such as auroral processes, lower atmospheric meteorological activity, and wave–mean flow interactions, can produce internal GWs.

[5]   GWs generated in the troposphere are found to cause plasma instabilities in the ionosphere [*Lee et al.*, 2008]. These studies motivate modelers to investigate possible dynamical effects of the disturbances in regions well above the turbopause. *Kazimirovsky et al.* [2003] and *Laštovička* [2006] emphasized the wide-reaching importance of lower atmospheric disturbances for atmospheric vertical coupling.

[6]   Besides observational data, computational experiments can provide useful insight into GW characteristics. Some numerical simulations have focused on the propagation and dissipation properties of GWs at ionospheric altitudes. For example, *Klostermeyer* [1972] attempted to describe the propagation of GWs in the thermosphere in a linearized hydrodynamic model, extending from 150 km upward. Coincident geographical and geomagnetic axes were used, which is not a realistic description of the atmosphere. Also, dynamical effects of GWs on the thermospheric mean flow were not studied. The possibility of dynamical forcing by GWs at thermospheric altitudes has been suggested by *Hines* [1974], but no specific modeling studies have been conducted. Further details on computational GW studies can be found in the work by *Yiğit et al.* [2008, and references therein].

[7]   GCMs were used to determine the effects of upwardly propagating small-scale GWs only up to the lower thermosphere because the parameterizations they employed lacked the appropriate representation of GW dissipation in the thermosphere, as mentioned above. Currently, most comprehensive middle atmosphere GCMs use an ad hoc GW damping above the MLT. For example, in the implementation of the Hines parameterization into the Extended Canadian Middle Atmosphere Model, *Fomichev et al.* [2002] have used an artificial exponential decay of GW drag above 105 km. In the Whole Atmosphere Community Climate Model extending from the surface up to ~145 km, *Garcia et al.* [2007] have incorporated only radiative and molecular diffusive damping into the GW scheme above 75 km. The HAMMONIA model [*Schmidt et al.*, 2006] fails to represent the propagation of GWs into the thermosphere realistically because the employed parameterization takes into account only a viscous correction due to increasing molecular diffusion. Most thermosphere models even entirely neglect the contribution of small-scale GWs to the energy and momentum budget of the upper atmosphere [e.g., *Richmond et al.*, 1992; *Zou et al.*, 2000; *Smithtro and Sojka*, 2005; *Tian et al.*, 2008].

[8]   We present an implementation of the extended GW drag parameterization from the stratosphere to *F* region altitudes into CMAT2 and simulations corresponding to the June solstice. The relative importance of GW drag in the thermosphere is discussed by comparing it to ion drag. Section 2 describes the CMAT2 GCM. Section 3 outlines the implementation of the extended GW drag parameterization into CMAT2. In section 4, the model configuration and experiment design are presented. The effects of dissipating GWs in the thermosphere on the zonal mean flow and the associated diurnal variations at June solstice are discussed in sections 5–9. In particular, in section 9 we demonstrate how the horizontal phase speed direction of a GW harmonic allows the latter to propagate to the *F* region seemingly avoiding filtering on its way up.

## 2.   Model Description

[9]   The Coupled Middle Atmosphere Thermosphere-2 (CMAT2) GCM is an updated version of the University College London (UCL) first generation CMAT model. CMAT was an extension of the three-dimensional Coupled Thermosphere-Ionosphere-Plasmasphere (CTIP) model [*Fuller-Rowell et al.*, 1996; *Millward et al.*, 1996]. A detailed description of CMAT is given by *Harris* [2001] and *Dobbin* [2005]. The current CMAT2 includes all the main parameterizations of the previous version. A number of updates to the dynamics and climatological distributions of chemical constituents were introduced to improve simulations in the middle and upper atmosphere. Note that the interactive chemistry was turned off in the runs to be presented here. Further details are given by *Cnossen et al.* [2009].

[10]   CMAT2 is a finite difference model solving the nonlinear Navier-Stokes equations on a global domain, which can extend from the lower stratosphere (100 hPa, or ~15 km) to the upper thermosphere (typically $1.43 \times 10^{-8}$ hPa, or ~250–600 km) with a variable latitude-longitude and/or height resolution. In our studies we have used a $2° \times 18°$ grid. Such a relatively high latitudinal resolution is needed, as it was a characteristic of previous thermospheric modeling studies [*Fuller-Rowell and Rees*, 1980; *Fuller-Rowell et al.*, 1996; *Millward et al.*, 1996]. CMAT2 has a variable height resolution, and we have used 63 pressure levels with one scale height vertical resolution at the top three levels, and 1/3 scale height vertical discretization everywhere below. The vertical levels are equidistant in log-pressure coordinates, corresponding to ~2 km resolution in the MLT, and 5 to 8 km near 190 km. This

resolution is typical for most middle atmosphere GCMs [e.g., *Schmidt et al.*, 2006].

[11] The model includes the absorption of solar radiation by ozone in the Chappuis, Huggins, and Hartley bands; by $O_2$ in the Schumann-Runge bands [*Strobel*, 1978], and the heating due to exothermic neutral chemistry. Middle atmosphere heating efficiencies are adopted according to *Mlynczak and Solomon* [1993]. Thermospheric heating, photodissociation, and photoionization are calculated for the absorption of solar X rays, extreme ultraviolet (EUV), and UV radiation between 1.8 and 184 nm using the SOLAR2000 empirical model of *Tobiska et al.* [2000]. Hard X-ray fluxes are adopted from the GLOW model [*Solomon et al.*, 1988; *Solomon and Abreu*, 1989].

[12] Radiative cooling parameterizations include the 5.3 $\mu$m NO emission [*Kockarts*, 1980], 63 $\mu$m fine structure atomic oxygen emission [*Bates*, 1951], local thermodynamic equilibrium (LTE) and non-LTE 15.6 $\mu$m $CO_2$ emission [*Fomichev et al.*, 1998], and $O_3$ 9.6 $\mu$m radiative emission [*Fomichev and Shved*, 1985]. In the simulations to follow, we use climatological distributions of chemical species. Accordingly, nitric oxide densities are taken from the Student Nitric Oxide Empirical Model (SNOEM) [*Marsh et al.*, 2004]. Ozone is taken from the UK Universities Global Atmospheric Modelling Programme (UGAMP) [*Li and Shine*, 1995]. Below the altitudes covered by SNOEM, NO and $NO_2$ are derived from observations of the HALogen Occultation Experiment (HALOE) instrument on board the UARS (Upper Atmosphere Research Satellite). O, $O_2$, and $N_2$ distributions are from the empirical MSISE-90 model [*Hedin*, 1991].

[13] In the atmosphere above ∼80 km, the importance of photoionization of atomic oxygen and dissociation of molecular oxygen increases. They contribute primarily to the formation of the charged atmosphere, the ionosphere. Photoionization and photodissociation processes release considerable amounts of heat in the thermosphere-ionosphere (TI) system. The impact of the ionosphere on the thermosphere system is significant. Charged particles that are confined to the Earth's magnetic field **B**, exert a drag force, the so-called ion drag, on the motion of neutral particles. Dissipating ionospheric currents provide Joule heating which can reach, depending on the geomagnetic activity, several hundreds to thousands of K $d^{-1}$ locally above 100 km. Both ion drag and Joule heating processes are included in CMAT2. We prescribe the morphology of the ionospheric electron density $n_e$ from the Parameterized Ionospheric Model (PIM) [*Daniell et al.*, 1995]. Thus, any direct dynamical feedback from the thermosphere to $n_e$ is excluded. The electric field strength is modeled after *Foster et al.* [1986]. Auroral particle precipitation at high latitudes is approximated by the TIROS/NOAA statistical model [*Fuller-Rowell and Evans*, 1987; *Codrescu et al.*, 1997]. The configuration and strength of the Earth's magnetic field is set according to the International Geomagnetic Reference Field (IGRF) [*Maus et al.*, 2005] as an offset tilted dipole field.

[14] Since CMAT2 lacks a troposphere, it is forced at the lower boundary (100 hPa) by two-dimensional NCEP reanalysis data [*Berg et al.*, 2007]. These data have been filtered to include wave numbers 1 to 3 nonzonal disturbances, which serve as a tropospheric source of planetary waves (PWs) in the model. To ensure a smooth day-to-day

transition, while the model is stepping forward in time, a cosine interpolation is used for the lower boundary fields. Tides play a crucial role in the dynamics and chemical composition of the atmosphere, in particular, in the lower thermosphere [*Groves and Forbes*, 1985], but their tropospheric generation is not fully represented in the model. Therefore, we prescribe tidal oscillations at the lower boundary from the global scale wave model (GSWM-02) [*Hagan and Forbes*, 2003]. They include the diurnal and semidiurnal components of migrating tides. Still, in the absence of sufficient tropospheric wave forcing, CMAT2 tends to produce stronger winter westerlies (more than 100 m $s^{-1}$) and a relatively cold winter lower stratosphere. This "cold bias" is an undesirable phenomenon, which affects all the mechanistic models that do not have tropospheres [*Hamilton et al.*, 1995; *Butchart and Austin*, 1998] as well as many full-scale GCMs [*Eyring et al.*, 2006]. It arises from a lack of mechanical forcing by both resolved and unresolved eddies in the stratosphere. In order to circumvent this problem we apply a weak Rayleigh drag, $-k_r\bar{u}$, in the altitude range between 25 and 65 km in all model simulations. The functional form of the Rayleigh friction coefficient is $k_r = k_{r0} \times \exp[(65 - z)/H]$, where $k_{r0}$ = 0.2 $s^{-1}$, and $H$ is the scale height.

## 3. Gravity Wave Drag Scheme Implementation

[15] In CMAT2, we implement the spectral GW drag parameterization developed by *Yiğit et al.* [2008] for GCMs extending into the thermosphere. This scheme systematically accounts for the dissipation of vertically propagating GWs due to molecular diffusion and thermal conductivity $\beta^i_{mol}$, ion drag $\beta^i_{ion}$, Newtonian cooling $\beta^i_{newt}$, and nonlinear breaking/saturation $\beta^i_{non}$ at every vertical model grid level, $\beta$ being the corresponding wave vertical damping rate, and $i$ denoting a specific harmonic in the spectrum. In the study presented here, we additionally take into account the dissipation due to the background atmospheric eddy viscosity, $\beta^i_{eddy}$ [*Meyer*, 1999],

$$\beta^i_{eddy} = \frac{2D_{eddy}N^3}{k_h(c_i - \bar{u})^4}, \qquad (1)$$

where $N^2 = (g/\theta)\partial\theta/\partial z$ is the Brunt-Väisälä frequency; $\theta$ is the potential temperature; $k_h = 2\pi/(300$ km$)$ is the horizontal wave number; and $c_i - \bar{u}$ is the intrinsic GW phase speed. The associated eddy diffusion coefficient $D_{eddy}$ was approximated by *Hagan et al.* [1995]. Note that the only feedback from the GW scheme into the model is the momentum deposition rate.

[16] For the calculations of ion drag effects on individual GW harmonics, $\beta^i_{ion}$, electron density profiles $n_e$ from PIM were used to evaluate the neutral-ion collision frequency $\nu_{ni}$. The total wave dissipation, $\beta^i_{tot} = \beta^i_{mol} + \beta^i_{newt} + \beta^i_{non} + \beta^i_{eddy} + \beta^i_{ion}$, is used in all the simulations to be presented. A full description of the dissipation rates can be found in the work by *Yiğit et al.* [2008]. Thermal effects of dissipating GWs are excluded in this study.

[17] First, an appropriate distribution of vertical flux of horizontal momentum (per unit mass) $\overline{u'w'}_i$, at the lower boundary (∼15 km) must be specified at all model latitude and longitude grid points. We assume the same spectral
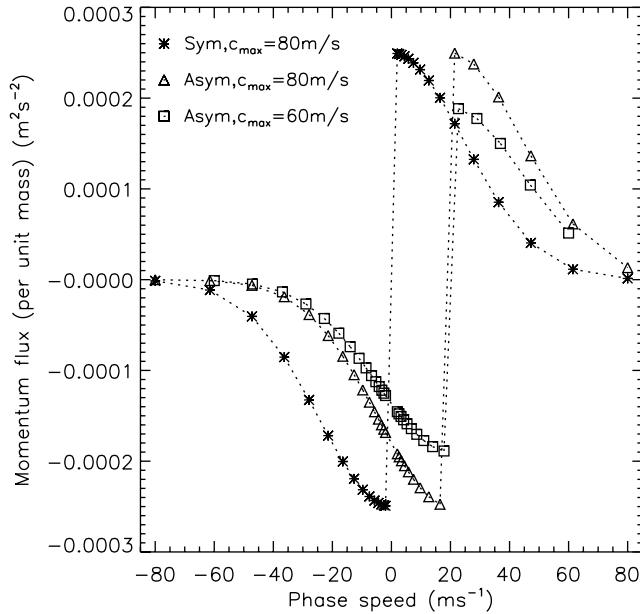
**Figure 1.** Momentum flux spectra at the source level. The asterisks, triangles, and rectangles denote the fluxes for individual harmonics used in EXP1/2/3/4. Other parameters are: $\overline{u'w'}_{max} = 0.00025$ m$^2$ s$^{-2}$ and $c_w = 35$ m s$^{-1}$. The connecting dotted lines highlight the Gaussian shape of the spectrum. Note that the flux amplitude in EXP4 is normalized with respect to EXP3. For the illustration of the asymmetric spectra, $\bar{u}_0 = 20$ m s$^{-1}$ is assumed.

Gaussian distribution of GW momentum flux at the source level as suggested by *Yiğit et al.* [2008],

$$\overline{u'w'}_i = \text{sgn}(c_i)\overline{u'w'}_{max} \exp\left[-(c_i/c_w)^2\right], \qquad (2)$$

where $\overline{u'w'}_{max}$ is the maximum momentum flux amplitude in the spectrum, and $c_w$ is the half width at half maximum of the Gaussian wave spectrum. It is illustrated in Figure 1 with $\overline{u'w'}_{max} = 2.5 \times 10^{-4}$ m$^2$ s$^{-2}$ and $c_w = 35$ m s$^{-1}$, where the asterisks connected by dotted lines mark the individual harmonics. The distribution of fluxes is symmetric with respect to $c = 0$ m s$^{-1}$; that is, the momentum flux values for the harmonics with $+c_i$ and $-c_i$ have same values. It is seen that slow harmonics have larger momentum fluxes, and the corresponding magnitudes decrease for faster harmonics. We adopt the anisotropic source spectrum which was shown to significantly improve the simulated general circulation in the middle atmosphere [*Medvedev et al.*, 1998]. For that, we assume that the horizontal phase velocities (both positive and negative) of GW harmonics are directed along the vector of the local mean wind at the source level. Therefore, spatial and temporal variations of the wind at the lower boundary determine the exact propagational characteristics of the parameterized GWs. We approximate the spectrum with 30 harmonics: 15 in each of the opposite directions. Their phase velocities are logarithmically distributed between $-c_{max}$ and $+c_{max}$, $c_{max}$ being the maximum phase velocity in the GW spectrum [*Medvedev and Klaassen*, 2000]. If otherwise not explicitly stated, $c_{max} = 80$ m s$^{-1}$ is used in simulations.

[18] Once GW fluxes are prescribed at the lower boundary, their vertical evolution and the resulting momentum flux divergences are calculated for all grid points in the vertical grid column. The details of the upward numerical integration are given by *Yiğit et al.* [2008, sect. 4]. The model time step is 40 s and the GW drag scheme is called every third time step.

## 4. Model Configuration and Experiment Design

[19] Before starting a model run on any given day, a start-up data set has to be generated. This is referred to as the spin-up process in which climatological distributions for chemical species and lower boundary configurations are taken from the MSISE-90 model [*Hedin*, 1991]. Then the model can be run either in a "perpetual" (diurnal cycle for a fixed model day only), or "daystepping" mode, in which the seasonal variations are also turned on. CMAT2 was first spun up for seven days for the perpetual 21 March 1985, and the output was used as an initial condition for all the numerical experiments presented here. Then the model was run in a daystepping mode until 6 July. Data were output every 6 hours during the last 21 days of the simulations (16 June to 6 July) for the diagnostics of the model climatology. For the study of the simulated diurnal variations on 22 June in section 9, extra output is produced every 30 min. The geomagnetic and solar activity were kept at constant low values ($F_{10.7} = 80 \times 10^{-22}$ W m$^{-2}$ Hz$^{-1}$; $K_p = 2^+$) throughout all model runs to eliminate additional uncertainties associated with the variability induced by solar and magnetospheric sources. The magnetospheric convection electric fields and the TIROS/NOAA particle precipitation parameterization use this constant geomagnetic activity index as an input, which corresponds to geomagnetically quiet conditions [*Foster et al.*, 1986]. In all simulations the same NCEP lower boundary forcing was used. Hence differences due to variations in PW activity were excluded from the numerical experiments.

[20] In the absence of GW drag CMAT2 tends to become computationally unstable. This instability can be avoided if very small time steps are used. The instability occurs because unrealistically large easterly and westerly jets develop in the middle atmosphere close to the solstice time. The temperature distribution in such simulations resembles radiative equilibrium. In EXP0, or the benchmark run, this lack of mechanical forcing was circumvented by applying an artificial Rayleigh drag in the mesosphere between 75 and 100 km (in addition to the stratospheric Rayleigh drag). Such drag was historically used by middle atmosphere GCMs to provide the necessary momentum deposition in the upper mesosphere, before more sophisticated GW drag schemes were developed [e.g., *Holton and Wehrbein*, 1980]. In EXP0, the vertical distribution of Rayleigh friction was set to $k_r^{MA} = k_{r0}^{MA} \times \exp[(z - 100)/27]$, where $k_{r0}^{MA} = 3$ s$^{-1}$, $z$ was given in km, and the superscript *MA* was introduced to distinguish this exponentially growing drag in the middle atmosphere from the decaying stratospheric drag described in section 2.

[21] In EXP1, the mesospheric Rayleigh friction was replaced with the GW drag scheme described in section 3. However, in order to single out the effects of GWs in the upper thermosphere, we cut off the momentum flux and the
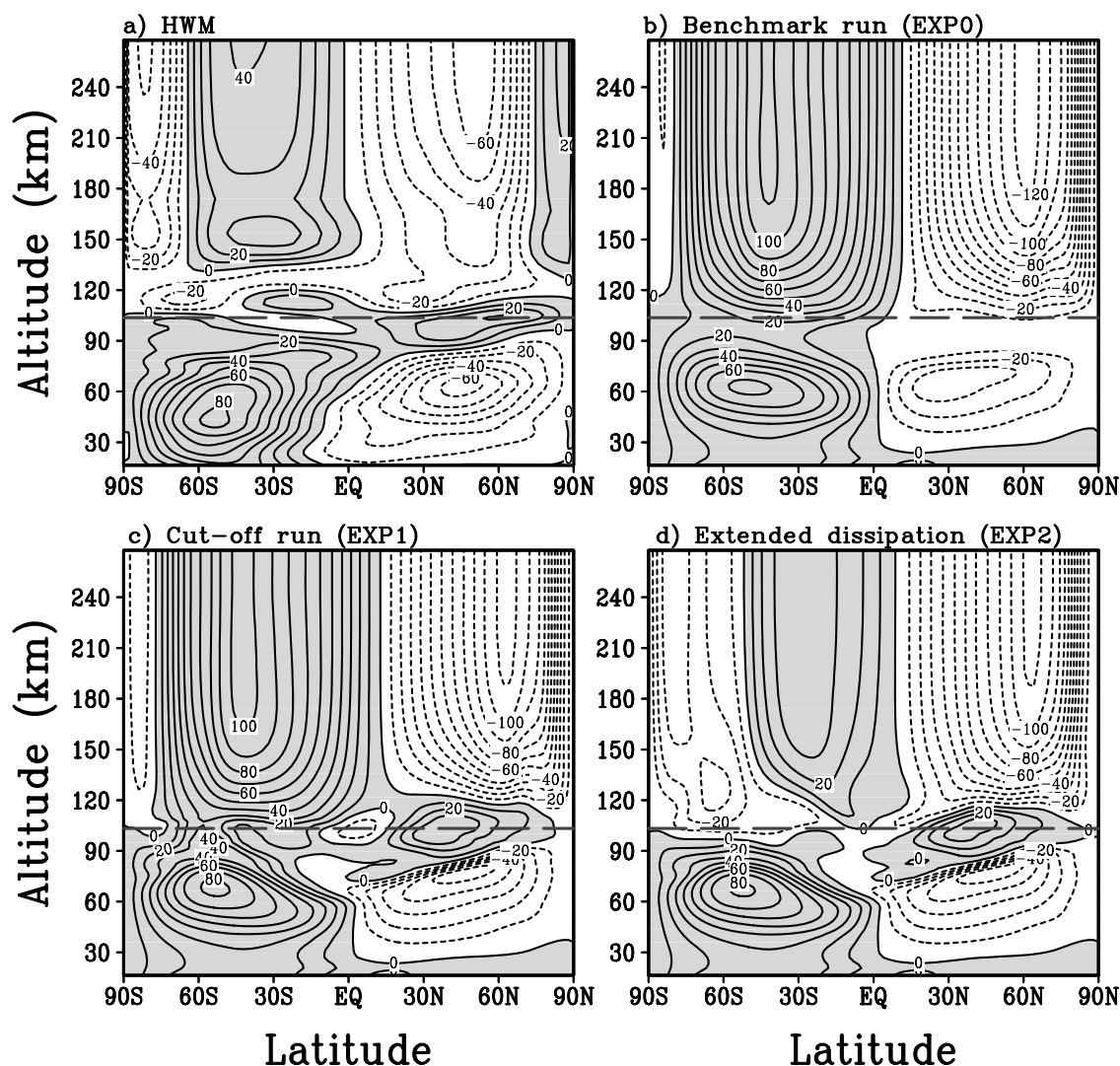
**Figure 2.** Height-latitude cross sections of the zonal mean zonal winds averaged over three weeks (16 June to 6 July). (a) HWM93. (b) EXP0: using the Rayleigh drag in the mesosphere. (c) EXP1: using the GW scheme up to ~105 km only. (d) EXP2: using GW drag in the whole model domain. Shaded areas with solid lines indicate eastward winds, and short-dashed lines show westward winds. The long-dashed line marks ~105 km. The contour intervals are 10 m s$^{-1}$.

associated GW momentum deposition above ~105 km. This run can also be viewed as imitating the use by thermospheric GCMs of conventional middle atmosphere GW drag schemes, or simplified upward extensions of them. The run that accounts for GW dissipation up to the model top (i.e., extended dissipation) is denoted here as EXP2. Other numerical experiments based on the variations of EXP2 are discussed further on in the text.

## 5. Mean Zonal Wind Simulations

[22] Most of the empirical models of the lower and middle atmosphere contain the information in the form of monthly mean fields. The output of middle atmosphere GCMs is often analyzed in the same form to compare with the empirical models. This practice of temporal averaging over certain periods is less common but also used by thermospheric modelers when mean quantities are to be presented. Figure 2 shows the zonal mean zonal winds from

15 km up to $F$ region heights, averaged over 21 days from 16 June to 6 July. These fields characterize the solstitial circulation, and exclude possible vacillations. Zonal wind data from the HWM93 [*Hedin et al.*, 1996] were processed and averaged in a similar manner to CMAT2 output to allow for a direct comparison with the model climatology, and are plotted in Figure 2a. Note that HWM93 is constructed from a wide range of observational sources such as incoherent scatter radars, MF and meteor radars, rocketsondes, gradient winds, and includes temporal and spatial variations. Despite numerous deficiencies, it currently describes the most established empirical climatology of horizontal winds in the thermosphere above the turbopause.

[23] For comparison, the zonal wind simulated using the mesospheric Rayleigh drag in the mesosphere (EXP0) is plotted in Figure 2b. Figure 2b demonstrates four distinct wind regimes in the strato-mesosphere, MLT, midlatitude and high-latitude TI, respectively. Westerly (easterly) jets dominate the winter (summer) hemispheres in the strato-
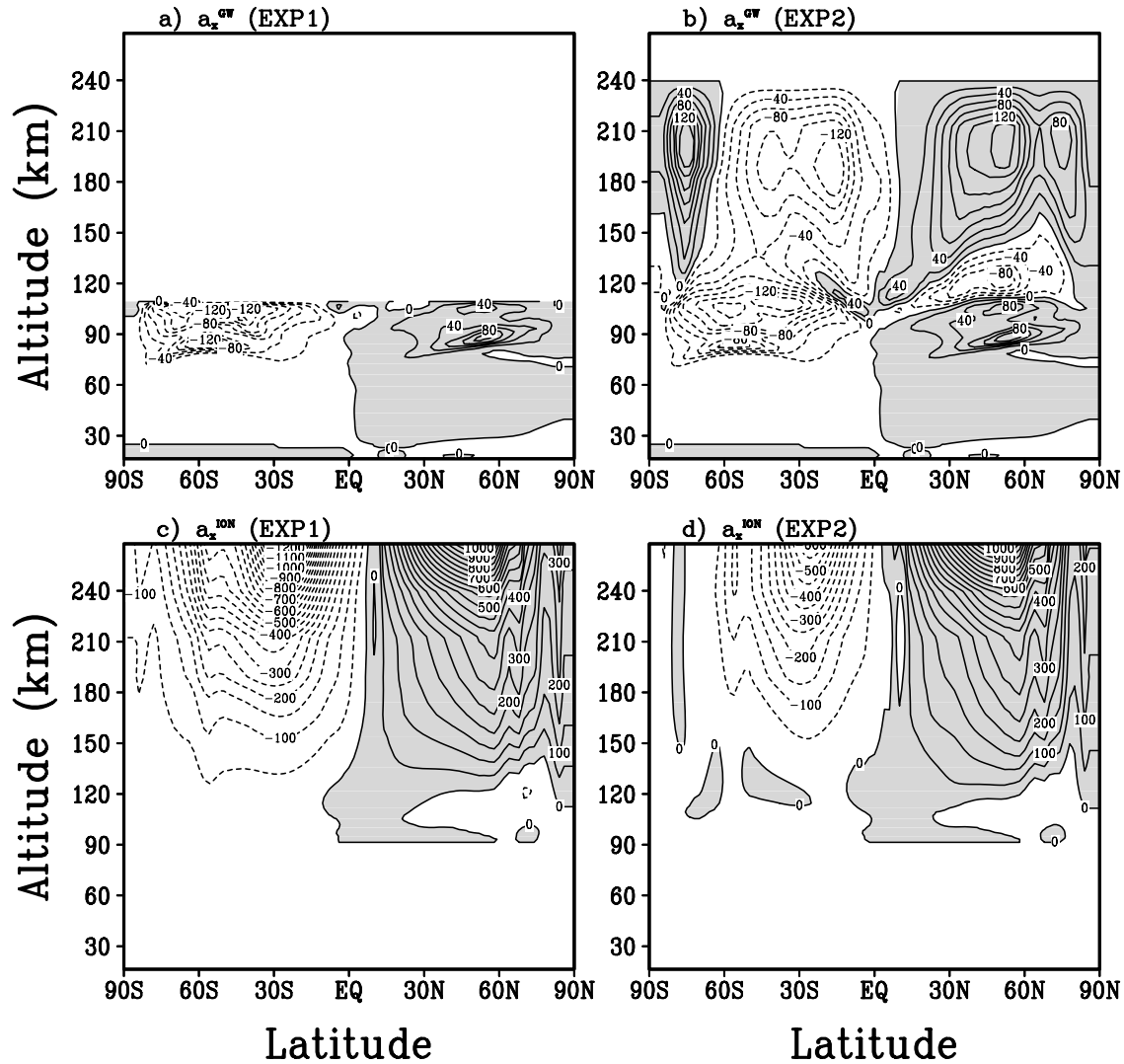
**Figure 3.** Height-latitude cross sections of the zonal mean zonal GW drag ($a_x^{GW}$) and ion drag ($a_x^{ION}$) in m s$^{-1}$ d$^{-1}$ averaged over three weeks corresponding to Figures 2c and 2d. (a) EXP1: GW drag cutoff above ~105 km. (b) EXP2: GW drag in the full model domain. Ion drag for (c) EXP1 and (d) EXP2. The contour intervals are 20 m s$^{-1}$ d$^{-1}$ and 50 m s$^{-1}$ d$^{-1}$ for the GW drag and ion drag panels, respectively.

mesosphere. These jets are formed by the Coriolis force acting upon the mean meridional pressure gradient directed, generally, from the hot summer hemisphere toward the colder winter hemisphere. The strato-mesospheric jets peak in midlatitudes at ~60–70 km in both hemispheres with magnitudes of ~80 and −60 m s$^{-1}$ in the HWM93 winter and summer hemispheres, respectively, and are somewhat weaker in the EXP0 simulations. In the MLT region, the zonal winds are reversed in the HWM93, which is not captured in the run with Rayleigh drag. Above this region, the EXP0 thermospheric winds increase with altitude, and reach maximum values of 110 and −120 m s$^{-1}$ at midlatitudes in both hemispheres, respectively. They have approximately zero vertical shears. A relatively weak (−10 m s$^{-1}$) easterly wind region is seen in the winter high latitudes between ~200 km and ~250 km. This feature is a consequence of the summer to winter meridional flow reversal associated with the high-latitude Joule heating and its enhancement by particle precipitation [*Dickinson et al.*, 1977; *Roble et al.*, 1977].

[24] It is seen that the EXP0 simulation in Figure 2b overestimates the magnitude of the thermospheric winds, and underestimates the high-latitude winter easterly reversal. Figure 2c shows the zonal mean zonal winds simulated with the GW momentum flux cut off close to the turbopause (EXP1). This artificially imposed limit completely eliminates the direct GW effects above ~105 km. Replacing the Rayleigh friction with more realistic GW drag significantly modifies the zonal mean circulation below ~105 km. The strato-mesospheric jets become more developed compared to the EXP0 case with peak values of ~80 and ~−50 m s$^{-1}$ in the winter and summer hemispheres, respectively, similar to the HWM93. There is a clear reversal of the summer easterly jet due to GW saturation. In particular, in the midlatitude MLT region, the peak value of ~30 m s$^{-1}$ is centered at around 100 km, which is close to the HWM93 climatology. Unlike the HWM93, no clear reversal occurs in the winter hemisphere. As one would expect from the fact that the GW drag cut off at ~105 km does not affect the upper atmosphere much, there are only minor changes in the

circulation of the TI between EXP0 and EXP1. Note that CMAT2 midlatitude thermospheric winds are overestimated in both EXP0 and EXP1 cases.

[25] The results of the application of the GW drag scheme in the full domain up to the model's top (EXP2) are shown in Figure 2d. Clear changes are seen in the mean zonal circulation of the upper atmosphere, which now resembles the HWM93 closer. The winter hemisphere midlatitude thermospheric westerlies of $\sim$30 m s$^{-1}$ are much weaker than in EXP0 and EXP1, and now are slightly smaller than in the HWM93. The high-latitude winter easterly TI winds extend down to the MLT and farther toward the equator with relatively large peak values of $\sim$$-30$ m s$^{-1}$ above 150 km. No apparent change is seen in the northern hemisphere (NH), although a closer examination shows slightly weaker thermospheric easterlies. Apart from a clearer reversal of the winter hemisphere MLT jets at $\sim$100 km due to the downward and equatorward extension of the easterly TI winds, there are minor changes in the middle atmosphere circulation.

[26] Overall, the results of EXP2 demonstrate a significant improvement of the model simulations with respect to the HWM93, compared to EXP0 and EXP1. They show that the dynamical effects of GWs propagating from below are nonnegligible in the thermosphere above the turbopause, and, in fact, play an important role in shaping the circulation of the upper thermosphere. The westward torque supplied by GWs in the winter hemisphere increases the apparent hemispheric asymmetry caused by the strong diabatic source in the high-latitude thermosphere associated with Joule heating and particle precipitation. In section 6 we take a closer look at GW forcing and compare it to ion drag, the established and important dynamical factor in the TI.

## 6. Mean Zonal Gravity Wave Drag

[27] Different forces affect the circulation at thermospheric heights: ion drag, advection, the pressure gradient force, and viscous drag are the dominant momentum sources [*Killeen and Roble*, 1984; *Kwak and Richmond*, 2007]. Several studies indicated a possible role of vertically propagating GWs [*Vadas and Fritts*, 2005; *Miyoshi and Fujiwara*, 2008], and now we are able to consider it quantitatively. The vertical cross sections of the mean zonal GW drag for EXP1 and EXP2 are shown in Figures 3a and 3b. Below the cutoff height of $\sim$105 km, both runs produce similar distributions of the GW drag with peak values of $-120$ and 100 m s$^{-1}$ d$^{-1}$ in the winter and summer hemispheres, correspondingly. It results from the preferential filtering of the westerly and easterly GW harmonics by the underlying strato-mesospheric jets, and is responsible for the wind reversals in the MLT. When waves are allowed to propagate higher (EXP2), they impose larger drag (up to $-140$ m s$^{-1}$ d$^{-1}$) immediately above the cutoff height in the winter hemisphere. This produces a fully developed wind reversal, as seen in Figure 2d. Further up in the TI, the associated GW drag is still nonnegligible; it reaches $-120$ and $+140$ m s$^{-1}$ d$^{-1}$ between 180 and 210 km, in the winter and summer hemisphere midlatitudes. It is predominantly directed against the mean wind, which explains the overall deceleration of the thermospheric jets. Again, this structure of the GW forcing can be explained by the filtering effect of the

strato-mesospheric jets in both hemispheres. In the high-latitude winter hemisphere, the eastward GW drag above $\sim$150 km is the result of the weaker dissipation of the surviving westerly propagating fast waves compared to their easterly counterpart harmonics. Since their intrinsic phase velocities, $|c_i - \bar{u}|$, are larger than those for $c_i < 0$ waves when $\bar{u} < 0$, these GWs deposit the westerly momentum upon reaching saturation/breaking conditions above 150 km. This case was described in more detail by *Yiğit et al.* [2008, sect. 7].

[28] Figures 3c and 3d demonstrate the distributions of the mean zonal ion drag in EXP1 and EXP2, respectively. It grows with height, and reaches $\pm$1000 m s$^{-1}$ d$^{-1}$ near the top of the model (Figure 3c). At midlatitudes, where ions are not accelerated to higher velocities by convection electric fields, neutrals constitute a momentum source for ions. Thus the bulk effect of the ion motion is to effectively decelerate the neutrals. Depending on the geomagnetic configuration and activity, the opposite effect may occur at high latitudes. The apparent asymmetry in the ion drag forcing is associated with the offset tilted dipole field configuration of the Earth's magnetic field. In the lower thermosphere, GW drag exceeds the ion friction. At 180 km, they have comparable magnitudes of about $\pm$100 m s$^{-1}$ d$^{-1}$ (Figures 3b and 3d). In the upper thermosphere, where the ionization rates are large, the mean ion drag dominates at almost all latitude sectors.

[29] Intercomparison of Figures 3c and 3d also shows that ion drag is reduced in the SH, where GW forcing has been found to affect the mean flow mostly. Deceleration of the mean flow, in particular at midlatitudes, by GW momentum deposition, modifies the distribution of ion drag, as the latter is proportional to the relative velocity between ions and neutrals.

## 7. Sensitivity to the Source Spectrum Variations

[30] Having shown significant GW effects in the thermosphere, we now turn to their sensitivity to variations of the source spectrum in the lower atmosphere. The limited scope of this paper allows us to consider only certain parameters that control the morphology of fluxes at the lower boundary. Offline calculations of *Yiğit et al.* [2008] demonstrated that the momentum deposition in the upper atmosphere is highly sensitive to the phase speed of the fastest harmonic, $c_{max}$, and to the shift of the spectral peak away from $c = 0$. Assigning the maximum of the momentum flux to the harmonic traveling with the wind speed at the source level appears to be representative and physically plausible, and was considered in the work by *Yiğit et al.* [2008] in more detail. Mathematically, this leads to the modification of the flux distribution (2) at the source level,

$$\overline{u'w'}_i = \text{sgn}(c_i - \bar{u}_0)\overline{u'w'}_{max} \exp\left[-(c_i - \bar{u}_0)^2/c_w^2\right], \quad (3)$$

where $\bar{u}_0 = \bar{u}(z \approx 15$ km$)$. We present two additional simulations, which differ from EXP2 only by specifications of the GW source. In experiment 3 (EXP3), the anisotropic source spectrum (2) of EXP2, which depends also on the direction of the mean wind at the launch height, is replaced with the anisotropic and "asymmetric" one (3), which depends on the magnitude of the background source wind as
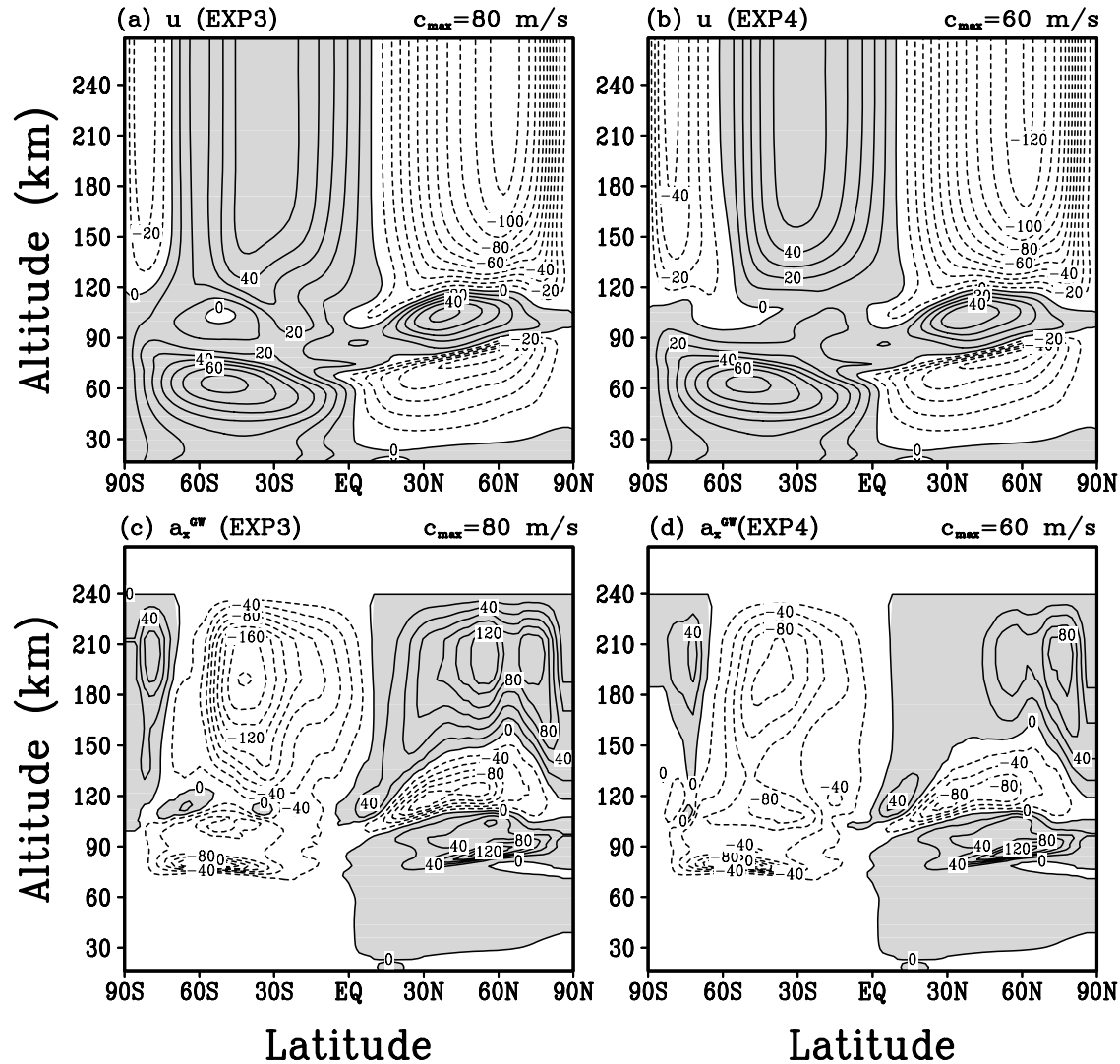
**Figure 4.** CMAT2 results with the asymmetric source spectrum (3) and two different spectral extents $c_{max}$. All other spectral parameters were kept the same as in EXP1 and EXP2. Zonal mean zonal winds with (a) $c_{max} = 80$ m s$^{-1}$ and (b) $c_{max} = 60$ m s$^{-1}$; (c and d) the associated GW drag distributions.

well, utilizing the same $c_{max} = 80$ m s$^{-1}$. Experiment 4 (EXP4) is similar to EXP3 except that $c_{max}$ is reduced to 60 m s$^{-1}$. The associated spectra are illustrated in Figure 1.

[31] Figures 4a and 4b display modeled mean zonal winds for EXP3 and EXP4, respectively. The associated GW drag is shown in Figures 4c and 4d. Notable changes in the simulated wind compared to EXP2 (Figure 2d) occur in the MLT region. The eastward reversals in the summer hemisphere have intensified (up to 50 m s$^{-1}$) in both EXP3 and EXP4, and become closer to the UARS (Upper Atmosphere Research Satellite) Reference Atmosphere Project (URAP) June zonal wind climatology [*Swinbank and Ortland*, 2003]. However, the westward reversals in the winter hemisphere disappear, much as in the cutoff run EXP1. Overall, the thermospheric winds have become more eastward compared to EXP2: the westerlies intensified and easterlies, generally, weakened. These phenomena are the consequence of the westerly bias in the GW momentum flux in the asymmetric spectrum (3) due to the predominant mean westerlies at the lower boundary. The thermospheric winds in the summer hemisphere are less sensitive to the

GW spectral asymmetry since the westerlies at the source level are weaker, and the bias is smaller than in the winter hemisphere. Stronger westerlies (and weaker easterlies) in the winter thermosphere produced by the westerly bias, in turn, allow harmonics with $c_i < 0$ to propagate higher, break or dissipate at larger amplitudes, and, therefore, to impose stronger torque on the less dense air. Figure 4c illustrates this with the peak value of $-180$ m s$^{-1}$ d$^{-1}$ in EXP3 compared to $-120$ m s$^{-1}$ d$^{-1}$ in EXP2. Reducing the number of fast harmonics in the spectrum by specifying $c_{max} = 60$ m s$^{-1}$ (EXP4) effectively weakens the described processes, and leads to more easterlies and less westerlies in the simulated thermospheric wind (Figures 4b and 4d).

[32] The above examples illustrate that the simulated circulation in the thermosphere, especially in the Southern Hemisphere (SH), is strongly affected by the momentum deposition owing to fast westward GW harmonics. In turn, the amount of momentum flux carried by these harmonics is significantly controlled by the spectral bias associated with the nonzero local wind at the source level in the troposphere. Overall, uncertainties in the specification of GW

**22 June, 00.00 UT, z~180 km**

**(a) T (EXP1)**

**(b) T (EXP2)**
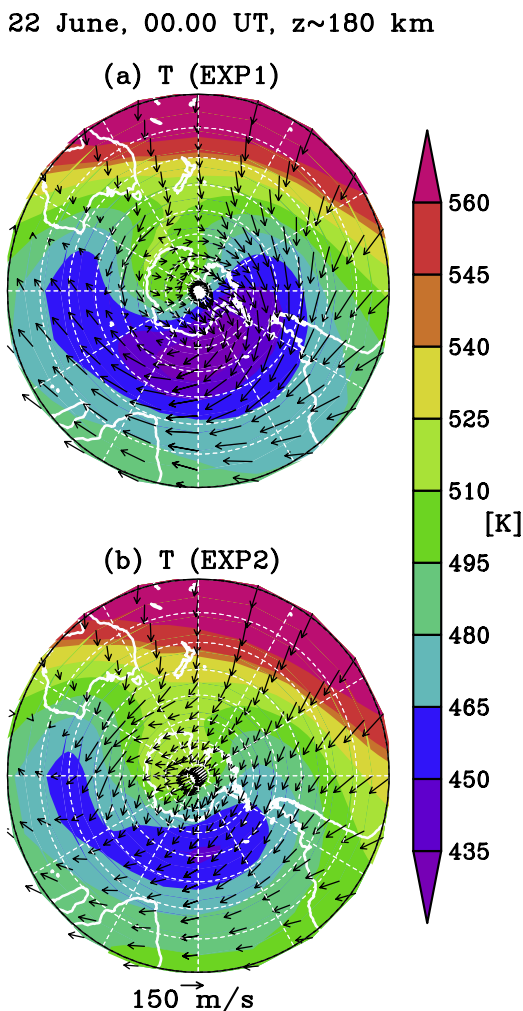
**Figure 5.** CMAT2 Southern Hemisphere (15°S–90°S) temperature fields (shaded) on 22 June (0000 UT) at ~180 km for (a) EXP1 and (b) EXP2. Arrows denote the horizontal wind distribution scaled with respect to 150 m s$^{-1}$ vector. White dashed lines illustrate different latitude and longitude sectors.

sources affect the results of simulations in the upper thermosphere in a manner similar to the well-known problem with slower GWs in the MLT.

## 8. Impact of GW Drag on the Circulation in the Southern Hemisphere

[33] As the most noticeable changes in the simulated circulation caused by GWs occur in the winter (southern in our case) hemisphere, we turn our attention on it in this section.

[34] Figures 3b and 3d suggest that GW drag is (in an average sense) more dominant than ion friction in the $E$ region; the opposite occurs in the $F$ region, and the two types of mechanical forcing are comparable around 180–210 km. Figure 5 presents the snapshots of the temperature (15°S to 90°S) in the SH at ~180 km simulated in EXP1 and EXP2 on 22 June (0000 UT). The horizontal wind is overplotted with vectors scaled with respect to the 150 m s$^{-1}$ arrow, as shown in Figure 5. Note that the longitude

connecting the South Pole with the bottom edge of the plot corresponds to the Greenwich Meridian, as in the rest of the polar stereographic plots in this paper.

[35] Three distinctive mechanisms determine the horizontal temperature structure at this height. The first is the seasonal gradient of the solar heating, which is responsible for the mean zonal temperature decrease from the summer Northern Hemisphere (NH) toward the SH, and from low to high latitudes in the SH, in particular. The second mechanism is associated with the strong gradients of the diabatic heating and cooling on the day and night sides, which is readily seen in the more than a hundred degree temperature difference (at 15°S–30°S) in Figure 5. The third mechanism is due to the high-latitude Joule heating and particle precipitation. It is manifested in the local temperature enhancement close to the pole on the noon side, which offsets the temperature minimum from the South Pole toward lower latitudes in the midnight sector. Accordingly, the wind in the SH has a complex pattern with strong eastward (clockwise in Figure 5) circumpolar flow in the dusk and night sector, and the superimposed cross-polar flow directed from the day to night side. The latter is directed against the dominant westerlies on the day and, especially, dawn side, where it actually reverses the circumpolar vortex. The winds near the local temperature maximum created by Joule heating and particle precipitation resemble an anticyclonic flow, which has the eastward direction at high latitudes.

[36] Inclusion of the GW drag in the thermosphere leads to significant modifications of the horizontal flow and, to some extent, of the temperature distribution (Figure 5b). Two main features distinguish EXP2 from EXP1: (1) The GW drag in the thermosphere weakens the westerly flow at the dusk and night side, and increases the easterly wind on the day and dawn side. In a zonally average sense, this results in the deceleration of the midlatitude eastward mean wind (see Figure 2d). At high latitudes, the anticyclonic flow is enhanced, especially on the dawn side, leading to the deeper westward reversal of the zonal mean wind. (2) EXP2 demonstrates higher (up to 30 K in zonal mean sense) winter polar temperature than in EXP1, and a few degrees colder summer pole (not shown here). The mechanism creating this change is very similar to the one near the mesopause. GW drag acting as an extratropical pump intensifies the meridional flow prompting stronger upwelling over the summer pole, and stronger downwelling over the winter pole. More detailed analysis (not presented here) shows that the temperature change, although small compared to thermospheric temperatures in CMAT2 and MSISE-90, is predominantly due to stronger adiabatic cooling in the NH and adiabatic heating in the SH. Other diabatic heating rates change little between EXP1 and EXP2.

[37] The effect of the GW drag can be seen quantitatively in Figures 6a and 6b, where the distributions of the zonal wind is plotted for EXP1 and EXP2. The midlatitude westerly winds on the night and dusk side are decelerated from more than 200 to about 120 m s$^{-1}$, the easterlies on the opposite side increase from −160 to −200 m s$^{-1}$, and the area covered by the easterlies broadens in the EXP2 run. The zonal GW drag itself and, for comparison, the ion drag in EXP2 are plotted in Figures 6c and 6d. It is seen that the GW drag is mostly negative, except in the high- and low-
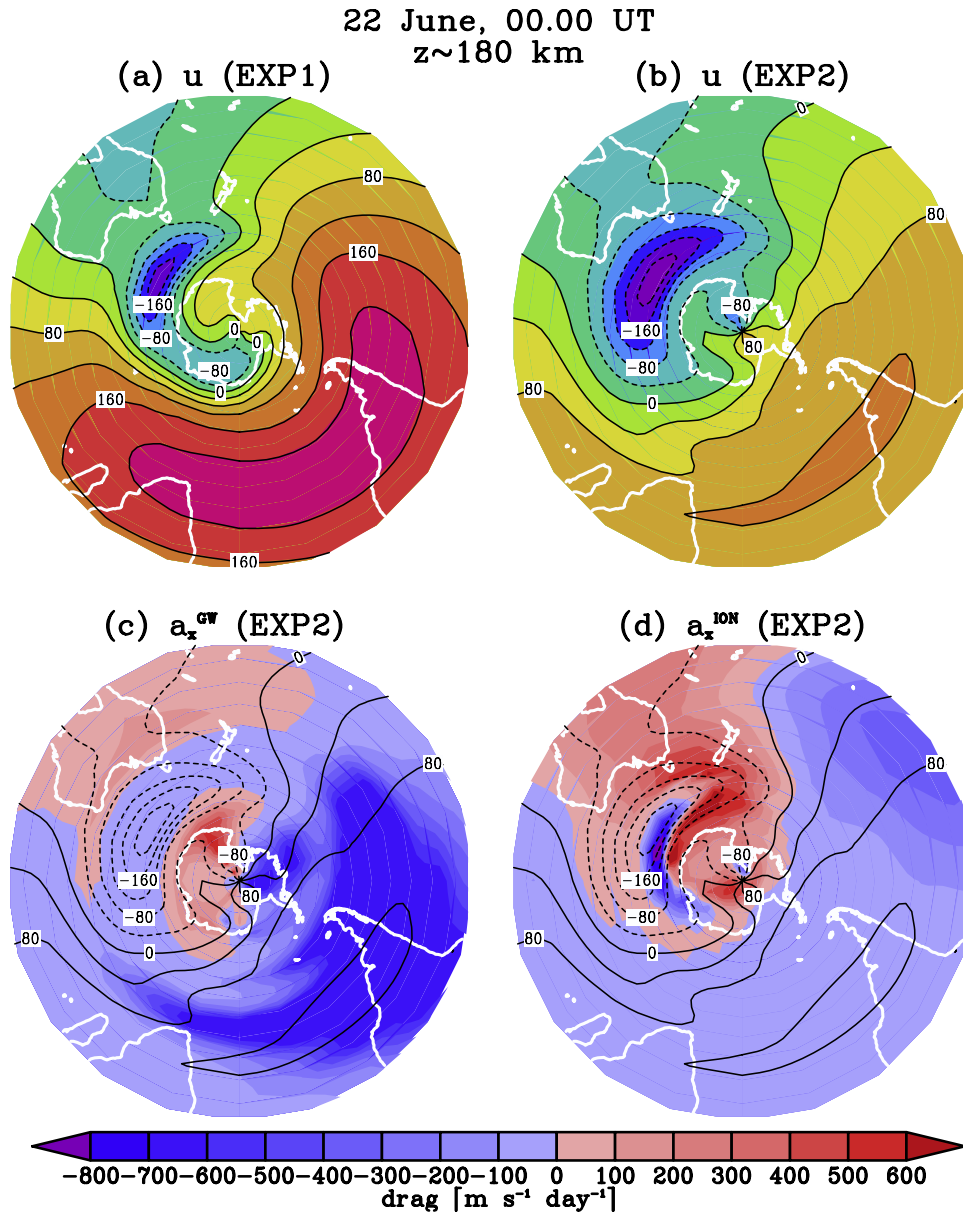
**Figure 6.** CMAT2 model zonal wind, GW drag and ion drag distributions over the SH (15°S−90°S) on 22 June (0000 UT) at ∼180 km. (a) Zonal wind with GW drag cut off. (b) Zonal wind with the GW scheme extended into the thermosphere. (c and d) Zonal GW and ion drag for the EXP2, respectively. Contour lines in Figures 6c and 6d show the zonal wind from Figure 6b.

latitude peaks of the dawn sector. The typical values are a few hundred m s$^{-1}$ d$^{-1}$, and can increase up to −700 m s$^{-1}$ d$^{-1}$. Although the drag is directed against the mean wind in most cases, locally it accelerates the westward flow in the dawn sector. The main effect of the ion drag is to decelerate the wind, and is particularly large in the dawn and noon sectors. Figures 6c and 6d clearly show that the GW drag is, at least, of the same order of magnitude or stronger than the ion drag, and should not be neglected at this height.

## 9. June Solstice Diurnal Variations

[38] Previous sections demonstrated that GWs emitted in the lower atmosphere are capable of propagating into the thermosphere and significantly modifying the mean circu-

lation of the SH. Now we investigate the diurnal variations in the zonal mean flow and the associated variability in the zonal GW forcing.

[39] Figure 7 illustrates the diurnal variations of CMAT2 zonal wind and GW drag on 22 June at three different geographical locations each situated on the Greenwich Meridian: 45°N (Figure 7a), 45°S (Figure 7b), and 75°S (Figure 7c). For simplicity, 45°N and 45°S will be referred to as the NH and SH, respectively, while 75°S will be termed as the high-latitude SH. In Figures 7a−7c, the drag distribution in m s$^{-1}$ d$^{-1}$ is color-shaded while the background mean flow is overplotted in black solid/dotted lines of 10 m s$^{-1}$ interval, indicating eastward/westward flow. We focus on the altitude range between 100 and 250 km.
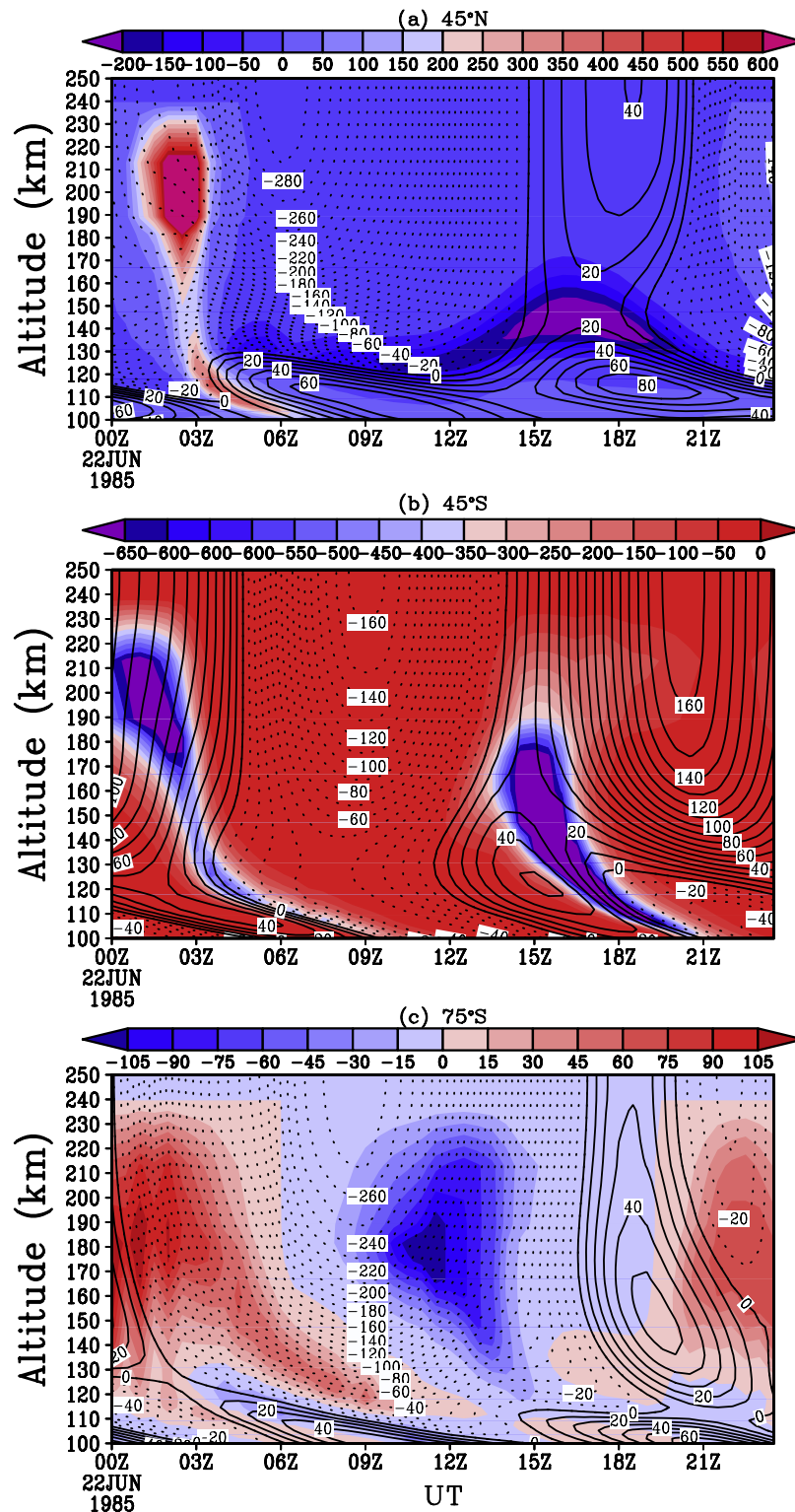
**Figure 7.** Diurnal variations of the zonal wind and zonal GW drag in EXP2 on 22 June at three different geographical locations situated on the Greenwich Meridian: (a) 45°N, (b) 45°S, and (c) 75°S. Color shading is the zonal GW drag (in m s$^{-1}$ d$^{-1}$). The contour solid/dotted lines show the eastward/westward zonal winds (in m s$^{-1}$).

0000 UT corresponds to local midnight, and 1200 UT is the local noon. We concentrate on these representative latitudes because our previous results have indicated significant GW activity there.

[40] A clear transition between the middle and upper atmosphere motions is seen at all latitudes. The downward phase progression with increasing local time characteristic of vertically propagating diurnal and semidiurnal tides
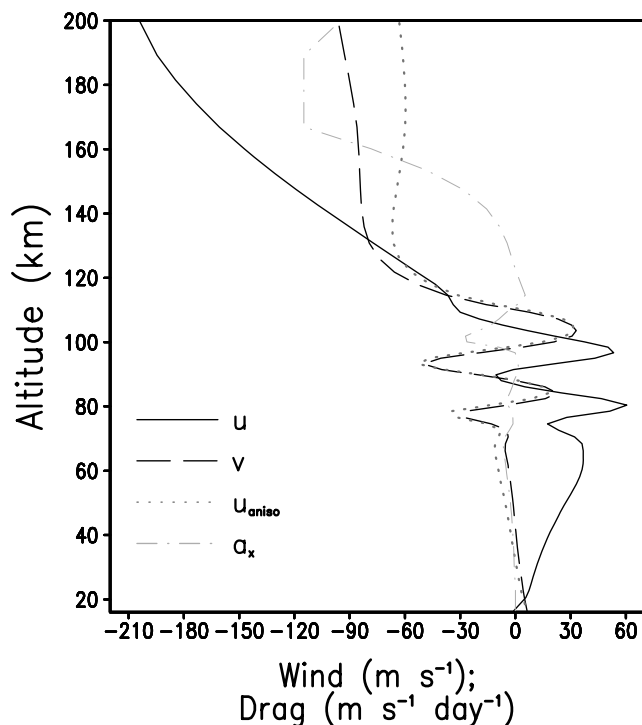
**Figure 8.** Vertical profiles of the zonal wind (solid line), meridional wind (dashed line), and their projections on the direction of GW propagation (dotted line) at the grid point on the Greenwich Meridian, 74°S at 1200 UT (22 June). The resultant zonal GW drag is plotted with the dash-dotted line.

occurs in the lower thermosphere with the semidiurnal oscillations penetrating higher. Above, in accordance with existing theoretical and observational expectations [e.g., *Forbes* 2007], the diurnal in situ generated tide with longer vertical wavelength and small wind shear due to the increased molecular viscosity dominates. Individual vertical profiles of the zonal GW drag at different UT exhibit large variability. In accordance with the average zonal GW drag in our previous results, eastward/westward GW forcing dominates in the NH/SH, effectively acting against the mean flow. At certain local times, GW drag extends up to 240 km. After local midnight, there are GW drag maxima of $\pm600$ m s$^{-1}$ d$^{-1}$ located typically between 180 and 210 km in both hemispheres. At later times, owing to the eastward MLT tidal winds, eastward GW drag in the NH diminishes. A relatively weak westward forcing around 140 km, $\sim-200$ m s$^{-1}$ d$^{-1}$, between 15 and 19 UT emerges. On the other hand, the SH diurnal GW drag variation shows a second strong peak of westward forcing extending up to 180 km.

[41] The high-latitude winter thermosphere from 100 to 250 km shown in Figure 7c illustrates a clear competition between the westward and eastward GW momentum deposition. The associated intensity of the GW forcing, $-100$ to $+100$ m s$^{-1}$ d$^{-1}$, is much smaller than at the midlatitudes in Figures 7a and 7b. There is an eastward drag at night, predominantly acting against the background wind, while the westward drag around local noon accelerates the background westward winds over a significant altitude range, from 130 to 230 km, with a peak value of $-100$ m s$^{-1}$ d$^{-1}$ at 180 km. Closer investigation of this feature provides a

new insight into the propagation of GWs into the thermosphere as a consequence of wave anisotropy. As discussed earlier, GW momentum fluxes associated with large phase speeds dominate at high altitudes. Since the source spectrum is symmetric, the peak of westward GW drag at noon can come only from fast westward traveling harmonics. The fastest westward harmonic launched in EXP2 is $c = -80$ m s$^{-1}$. On the other hand, the mean zonal wind continuously increases from 0 to $-210$ m s$^{-1}$ between 100 and 200 km at noon, as seen in Figure 7c. This means that all the harmonics moving to the west should have met their respective critical levels and been filtered out below $\sim130$ km. (Note that GW schemes of this kind imply that harmonics propagate upward without leaving the model vertical grid columns, as discussed in the work by *Yiğit et al.* [2008].) How can wave propagation up to $F$ region altitudes occur under these circumstances?

[42] The anisotropic GW source spectrum is the key mechanism, and Figure 8 illustrates this effect in detail for an individual CMAT2 grid column at 75°S during local noon. The zonal and meridional model winds at the source level at this geographical point are $\bar{u}_0 \approx -1$ m s$^{-1}$ and $\bar{v}_0 \approx 6.3$ m s$^{-1}$, correspondingly. This implies that the wind vector and therefore the direction of the generated waves are strongly tilted northwestward. Only the projection of the mean wind on this direction affects the propagation of wave harmonics. The zonal, meridional, and the projected wind from the model are plotted in Figure 8. It is seen that the background wind "perceived" by GW harmonics is significantly weaker than the zonal wind alone, and allows fast waves with $c < 0$ to propagate into the $F$ region. For example, at $\sim180$ km $\bar{u} \approx -184$ m s$^{-1}$ and $\bar{v} \approx -90$ m s$^{-1}$, whereas the sum of their projections onto the direction of wave propagation yields only $\sim-60$ m s$^{-1}$. Therefore, fast harmonics can avoid filtering on their way up, grow in amplitude, and deposit the momentum at high altitudes. The green dash-dotted line in Figure 8 shows the projection of the resultant drag onto the west-east direction.

[43] The results of this section demonstrate that GW propagation and dissipation in the upper thermosphere are highly variable phenomena, and that the corresponding GW drag can noticeably affect the mean flow at least up to 230 km. If the horizontal direction of propagation of GW harmonics is not fixed and varies at the source level ("anisotropic" spectrum), they can sometimes penetrate much higher than one would commonly expect in the presence of strong background wind, and affect the layers there.

## 10. Summary and Conclusions

[44] A nonlinear spectral gravity wave drag parameterization suitable for the thermosphere developed by *Yiğit et al.* [2008] has been implemented into the UCL CMAT2 general circulation model. Results of simulations for the June solstice have been validated against the Horizontal Wind Model (HWM93). These were compared with those from the runs without the GW scheme and with the GW momentum deposition cut off above 105 km. The latter experiment was mimicking an ad hoc suppression of GW momentum fluxes above the turbopause, adopted by many thermospheric GCMs that implement GW drag schemes designed for middle atmosphere models.

[45] It has been found that, under June solstice conditions, GWs propagating from the lower atmosphere have large dynamical effects on the mean flow in the $F$ region. These effects are particularly strong in the winter (southern) hemisphere, where the westward momentum deposited by GWs significantly weakens the westerlies, and enhances the high-latitude easterlies above the turbopause, in accordance with the HWM93. As in the middle atmosphere, the dynamical response of the upper thermosphere is sensitive to variations of the GW source spectrum. However, the source specifications commonly used in middle atmosphere GCMs allow the reproduction of the circulation both near the mesopause and in the upper thermosphere to be reasonably good.

[46] The deposited GW momentum is predominantly directed against the mean wind, much like the effect of the midlatitude ion drag, but locally it can accelerate the flow, too. Magnitudes of the GW drag (hundreds of m s$^{-1}$ d$^{-1}$) exceed those of the ion drag immediately above the turbopause, and are comparable at least up to $F$ region altitudes ($\sim$180–200 km). Inclusion of GWs in the upper thermosphere decelerates the simulated flow, and hence weakens ion drag.

[47] The study of the diurnal cycle of the GW drag and zonal winds have shown that wave propagation into the upper thermosphere is highly variable, and can sometimes lead to counterintuitive local effects. Since the Earth's geomagnetic axis does not coincide with its geographical axis, the thermospheric high-latitude mean winds exhibit strong local/universal time variations. Section 9 has described an example of acceleration of the mean flow around local noon by GW harmonics, which seemingly avoided filtering on their way up to 200–220 km. Despite the apparently large zonal wind, this effect can take place when the wave source is anisotropic, and the mean wind projected onto the direction of wave propagation still remains favorable at all heights for harmonics to penetrate into the upper thermosphere.

[48] This numerical study has shown that proper accounting for dissipative mechanisms in the GW parameterization generates a considerable body forcing in the simulated upper thermosphere. The dynamical effects of GWs originating in the lower atmosphere are not only nonnegligible above the turbopause, but are comparable to the effects of ion drag up to at least 180–200 km. Further observational constraints on the GW momentum fluxes are required to quantify the dynamical coupling of the lower atmosphere and the thermosphere-ionosphere region.

## References

Alexander, M. J., et al. (2008), Global estimates of gravity wave momentum flux from High Resolution Dynamics Limb Sounder observations, *J. Geophys. Res.*, *113*, D15S18, doi:10.1029/2007JD008807.

Allen, S. J., and R. A. Vincent (1995), Gravity wave activity in the lower atmosphere: Seasonal and latitudinal variations, *J. Geophys. Res.*, *100*, 1327–1350.

Bates, D. R. (1951), The temperature of the upper atmosphere, *Proc. Phys. Soc.*, *64B*, 805–821.

Becker, E., and D. C. Fritts (2006), Enhanced gravity wave activity and interhemispheric coupling during the MaCWAVE/MIDAS northern summer program 2002, *Ann. Geophys.*, *24*, 1175–1188.

Berg, P., B. Christiansen, P. Thejll, and N. Arnold (2007), The dynamical response of the middle atmosphere to the tropospheric solar signal, *J. Geophys. Res.*, *112*, D20122, doi:10.1029/2006JD008237.

Berger, U. (2008), Modeling of middle atmosphere dynamics with LIMA, *J. Atmos. Sol. Terr. Phys.*, *70*, 1170–1200.

Butchart, N., and J. Austin (1998), Middle atmosphere climatologies from the troposphere-stratosphere configuration of the UKMO's Unified Model, *J. Atmos. Sci.*, *55*, 2782–2809.

Cnossen, I., M. J. Harris, N. F. Arnold, and E. Yiğit (2009), Modelled effect of changes in the $CO_2$ concentration on the middle and upper atmosphere: Sensitivity to gravity wave parameterization, *J. Atmos. Sol. Terr. Phys.*, doi:10.1016/j.jastp.2008.09.014, in press.

Codrescu, M. V., T. J. Fuller-Rowell, R. G. Roble, and D. S. Evans (1997), Medium energy particle precipitation influences on the mesosphere and lower thermosphere, *J. Geophys. Res.*, *102*, 19,977–19,987.

Daniell, R. E., L. D. Brown, D. N. Anderson, M. W. Fox, P. H. Doherty, D. T. Decker, J. J. Sojka, and R. W. Schunk (1995), PIM: A global ionospheric parameterization based on first principles models, *Radio Sci.*, *30*, 1499–1510.

Dickinson, R. E., E. C. Ridley, and R. G. Roble (1977), Meridional circulation in the thermosphere. II. Solstice conditions, *J. Atmos. Sci.*, *34*, 178–192.

Djuth, F. T., M. P. Sulzer, S. A. Gonzales, J. D. Mathews, J. H. Elder, and R. L. Walterscheid (2004), A continuum of gravity waves in the Arecibo thermosphere?, *Geophys. Res. Lett.*, *31*, L16801, doi:10.1029/2003GL019376.

Dobbin, A. L. (2005), Modelling studies of possible coupling mechanisms between the upper and middle atmosphere, Ph.D. Thesis, Univ. of London, London.

Ern, M., P. Preusse, M. J. Alexander, and C. D. Warner (2004), Absolute values of gravity wave momentum flux derived from satellite data, *J. Geophys. Res.*, *109*, D20103, doi:10.1029/2004JD004752.

Eyring, V., et al. (2006), Assessment of temperature, trace species, and ozone in chemistry climate model simulations of the recent past, *J. Geophys. Res.*, *111*, D22308, doi:10.1029/2006JD007327.

Fomichev, V. I., and G. M. Shved (1985), Parameterization of the radiative flux divergence in the 9.6 $\mu$m $O_3$ band, *J. Atmos. Terr. Phys.*, *47*, 1037–1049.

Fomichev, V. I., J. P. Blanchet, and D. S. Turner (1998), Matrix parameterization of the 15 $\mu$m band cooling in the middle and upper atmosphere for variable $CO_2$ concentration, *J. Geophys. Res.*, *103*, 11,505–11,528.

Fomichev, V. I., W. E. Ward, S. R. Beagley, C. McLandress, J. C. McConnell, N. A. McFarlane, and T. G. Shepherd (2002), Extended Canadian Middle Atmosphere model: Zonal-mean climatology and physical parameterizations, *J. Geophys. Res.*, *107*(D10), 4087, doi:10.1029/2001JD000479.

Forbes, J. M. (2007), Dynamics of the upper mesosphere and thermosphere, *J. Meteorol. Soc. Jpn.*, *85B*, 193–213.

Foster, J. C., J. M. Holt, R. G. Musgrove, and D. S. Evans (1986), Ionospheric convection associated with discrete levels of particle precipitation, *Geophys. Res. Lett.*, *13*, 656–659.

Fuller-Rowell, T. J., and D. Rees (1980), A three-dimensional time-dependent model of the thermosphere, *J. Atmos. Sci.*, *37*, 2545–2567.

Fuller-Rowell, T. J., and D. S. Evans (1987), Height-integrated Pederson and Hall conductivity patterns inferred from the TIROS-NOAA satellite data, *J. Geophys. Res.*, *92*, 7606–7618.

Fuller-Rowell, T. J., D. Rees, S. Quegan, R. J. Moffett, M. V. Codrescu, and G. H. Millward (1996), A Coupled Thermosphere-Ionosphere Model (CTIM), in *Solar-Terrestrial Energy Program: Handbook of Ionospheric Models*, edited by R. W. Schunk, pp. 217–238, Utah State Univ., Logan.

Garcia, R. R., D. R. Marsh, D. E. Kinnison, B. A. Boville, and F. Sassi (2007), Simulations of secular trends in the middle atmosphere, *J. Geophys. Res.*, *112*, D09301, doi:10.1029/2006JD007485.

Groves, G. V., and J. M. Forbes (1985), Mean zonal and meridional accelerations and mean heating induced by solar tides for equinox and solstice, *Planet. Space Sci.*, *33*, 283–293.

Hagan, M. E., and J. M. Forbes (2003), Migrating and nonmigrating semidiurnal tides in the middle and upper atmosphere excited by tropospheric latent heat release, *J. Geophys. Res.*, *108*(A2), 1062, doi:10.1029/2002JA009466.

Hagan, M. E., J. M. Forbes, and F. Vial (1995), On modeling migrating solar tides, *Geophys. Res. Lett.*, *22*, 893–896.

Hamilton, K., R. J. Wilson, J. D. Mahlman, and L. J. Umscheid (1995), Climatology of SKYHI Troposphere-Stratosphere-Mesosphere General Circulation Model, *J. Atmos. Sci.*, *52*, 5–43.

Harris, M. J. (2001), A new coupled middle atmosphere and thermosphere circulation model: Studies of dynamic, energetic and photochemical coupling in the middle and upper atmosphere, Ph.D. Thesis, Univ. of London, London.

Hedin, A. E. (1991), Extension of the MSIS thermosphere model into the middle and lower atmosphere, *J. Geophys. Res.*, *96*, 1159–1172.

Hedin, A. E., et al. (1996), Empirical wind model for the upper, middle and lower atmosphere, *J. Atmos. Terr. Phys.*, *58*, 1421–1447.

Hines, C. O. (1974), Momentum deposition by atmospheric waves and its effects on the thermospheric circulation, in *The Upper Atmosphere in Motion: A Selection of Papers With Annotation*, Geophys. Monogr. Ser., vol. 18, edited by C. O. Hines, pp. 760–764, AGU, Washington, D. C.

Holton, J. R., and W. M. Wehrbein (1980), A numerical model of the zonal mean circulation of the middle atmosphere, *Pure Appl. Geophys.*, *118*, 284–306.

Janches, D., D. C. Fritts, D. M. Riggin, M. P. Sulzer, and S. Gonzales (2006), Gravity waves and momentum fluxes in the mesosphere and lower thermosphere using 430 MHz dual-beam measurements at Areibo: 1. Measurements, methods, and gravity waves, *J. Geophys. Res.*, *111*, D18107, doi:10.1029/2005JD006882.

Kazimirovsky, E., M. Herraiz, and B. A. D. L. Morena (2003), Effects on the ionosphere due to phenomena occuring from below, *Surv. Geophys.*, *24*, 134–184.

Killeen, T. L., and R. G. Roble (1984), An analysis of the high-latitude thermospheric wind pattern calculated by a thermospheric general circulation model: 1. Momentum forcing, *J. Geophys. Res.*, *89*, 7509–7522.

Klostermeyer, J. (1972), Numerical calculation of gravity wave propagation in a realistic thermosphere, *J. Atmos. Terr. Phys.*, *34*, 765–774.

Kockarts, G. (1980), Nitric oxide cooling in the terrestrial thermosphere, *Geophys. Res. Lett.*, *7*, 137–140.

Kwak, Y.-S., and A. D. Richmond (2007), An analysis of the momentum forcing in the high-latitude lower thermosphere, *J. Geophys. Res.*, *112*, A01306, doi:10.1029/2006JA011910.

Laštovička, J. (2006), Forcing of the ionosphere by waves from below, *J. Atmos. Sol. Terr. Phys.*, *68*, 479–497.

Lee, M. C., R. Pradipta, W. J. Burke, A. Labno, L. M. Burton, J. A. Cohen, S. E. Dorfman, A. J. Coster, M. P. Sulzer, and S. P. Kuo (2008), Did tsunami-launched gravity waves trigger ionospheric turbulence over Arecibo?, *J. Geophys. Res.*, *113*, A01302, doi:10.1029/2007JA012615.

Li, D., and K. P. Shine (1995), A 4-dimensional ozone climatology for UGAMP models, Internal Rep. 35, U.K. Univ. Global Atmos. Modell. Programme, Reading, U. K.

Livneh, D. J., I. Seker, F. T. Djuth, and J. D. Mathews (2007), Continuous quasiperiodic thermospheric waves over Arecibo, *J. Geophys. Res.*, *112*, A07313, doi:10.1029/2006JA012225.

Marsh, D. R., S. C. Solomon, and A. E. Reynolds (2004), Empirical model of nitric oxide in the lower thermosphere, *J. Geophys. Res.*, *109*, A07301, doi:10.1029/2003JA010199.

Maus, S. S., et al. (2005), The 10th generation international geomagnetic reference field, *Phys. Earth Planet. Inter.*, *151*, 320–322.

Medvedev, A. S., and G. P. Klaassen (2000), Parameterization of gravity wave momentum deposition based on nonlinear wave interactions: Basic formulation and sensitivity tests, *J. Atmos. Sol. Terr. Phys.*, *62*, 1015–1033.

Medvedev, A. S., G. P. Klaassen, and S. R. Beagley (1998), On the role of an anisotropic gravity wave spectrum in maintaining the circulation of the middle atmosphere, *Geophys. Res. Lett.*, *25*, 509–512.

Meyer, C. K. (1999), Gravity wave interactions with mesospheric planetary waves: A mechanism for penetration into the thermosphere-ionosphere system, *J. Geophys. Res.*, *104*, 28,181–28,196.

Millward, G., R. J. Moffett, S. Quegan, and T. J. Fuller-Rowell (1996), A Coupled Thermosphere-Ionosphere-Plasmasphere Model (CTIP), in *Solar-Terrestrial Energy Program: Handbook of Ionospheric Models*, edited by R. W. Schunk, pp. 239–279, Utah State Univ., Logan.

Mitchell, N. J., and V. S. C. Howells (1998), Vertical velocities associated with gravity waves measured in the mesosphere and lower thermosphere with the EISCAT VHF radar, *Ann. Geophys.*, *16*, 1367–1379.

Mitchell, N. J., L. Thomas, and I. T. Prihard (1994), Gravity waves in the stratosphere and troposphere observed by lidar and MST radar, *J. Atmos. Terr. Phys.*, *56*, 939–947.

Miyoshi, Y., and H. Fujiwara (2008), Gravity waves in the thermosphere simulated by a general circulation model, *J. Geophys. Res.*, *113*, D01101, doi:10.1029/2007JD008874.

Mlynczak, M. G., and S. Solomon (1993), A detailed study of heating efficiency in the middle atmosphere, *J. Geophys. Res.*, *98*, 10,517–10,541.

Oliver, W. L., Y. Otsuka, M. Sato, T. Takami, and S. Fukao (1997), A climatology of *F* region gravity wave propagation over the middle and upper atmosphere radar, *J. Geophys. Res.*, *102*, 14,499–14,512.

Richmond, A. D., E. C. Ridley, and R. G. Roble (1992), A thermosphere/ionosphere general circulation model with coupled electrodynamics, *Geophys. Res. Lett.*, *19*, 601–604.

Roble, R. G., R. E. Dickinson, and E. C. Ridley (1977), Seasonal and solar cycle variations of the zonal mean circulation in the thermosphere, *J. Geophys. Res.*, *82*, 5493–5504.

Schmidt, H., G. P. Brasseur, M. Charron, E. Manzini, M. A. Giorgetta, and T. Tiehl (2006), The HAMMONIA Chemistry Climate Model: Sensitivity of the mesopause region to the 11-year solar cycle and $CO_2$ doubling, *J. Clim.*, *19*, 3903–3931.

Smithtro, C. G., and J. J. Sojka (2005), A new global average model of the coupled thermosphere and ionosphere, *J. Geophys. Res.*, *110*, A08305, doi:10.1029/2004JA010781.

Solomon, S. C., and V. Abreu (1989), The 630-nm dayglow, *J. Geophys. Res.*, *94*, 6817–6824.

Solomon, S. C., P. B. Hayes, and V. Abreu (1988), The auroral 6300 Å emission: Observations and modeling, *J. Geophys. Res.*, *93*, 9867–9882.

Strobel, D. F. (1978), Parameterization of the atmospheric heating rate from 15 to 120 km due to $O_2$ and $O_3$ absorption of solar radiation, *J. Geophys. Res.*, *83*, 6225–6230.

Swinbank, R., and D. A. Ortland (2003), Compilation of wind data for the Upper Atmosphere Research Satellite (UARS) Reference Atmosphere Project, *J. Geophys. Res.*, *108*(D19), 4615, doi:10.1029/2002JD003135.

Tian, F., J. F. Kasting, H. Liu, and R. G. Roble (2008), Hydrodynamic planetary thermosphere model: 1. Response of the Earth's thermosphere to extreme solar EUV conditions and the sginificance of adiabatic cooling, *J. Geophys. Res.*, *113*, E05008, doi:10.1029/2007JE002946.

Tobiska, W. K., T. Woods, F. Eparvier, R. Viereck, L. Floyd, D. Bouwer, G. Rottman, and O. R. White (2000), The SOLAR2000 empirical solar irradiance model and forecast tool, *J. Atmos. Sol. Terr. Phys.*, *62*, 1233–1250.

Vadas, S. L., and D. C. Fritts (2005), Thermospheric responses to gravity waves: Influences of increasing viscosity and thermal diffusivity, *J. Geophys. Res.*, *110*, D15103, doi:10.1029/2004JD005574.

Yang, G., B. Clemesha, P. Batista, and D. Simonich (2008), Lidar study of the characteristics of gravity waves in the mesopause region at a southern low-latitude location J, *Atmos. Sol. Terr. Phys.*, *70*, 991–1011.

Yiğit, E., A. D. Aylward, and A. S. Medvedev (2008), Parameterization of the effects of vertically propagating gravity waves for thermosphere general circulation models: Sensitivity study, *J. Geophys. Res.*, *113*, D19106, doi:10.1029/2008JD010135.

Zou, L., I. C. F. Müller-Wodarg, A. D. Aylward, G. H. Millward, T. J. Fuller-Rowell, D. W. Idenden, and R. J. Moffett (2000), Annual and semiannual variations in the ionospheric F2-layer. I. Modelling, *Ann. Geophys.*, *18*, 927–944.

————————————

A. D. Aylward, M. J. Harris and E. Yiğit, Department of Physics and Astronomy, University College London, Gower Street, London WC1E 6BT, UK. (alan@apl.ucl.ac.uk; matthew@regolith.org; erdal@apl.ucl.ac.uk)

P. Hartogh and A. S. Medvedev, Max Planck Institute for Solar System Research, D-37191 Katlenburg-Lindau, Germany. (hartogh@mps.mpg.de; medvedev@mps.mpg.de)